Direct Observation and Analysis of CuO_2 Shear Defects in $La_{2-x}Sr_xCuO_4$

PRATIBHA L. GAI AND EUGENE M. MCCARRON III

Direct observations of CuO_2 sheet defect structures in superconducting $La_{2-x}Sr_xCuO_4$, with x in the range $0.05 \leq x \leq 0.15$, are reported. Electron microscopy shows that extended line defects are generated in {010} planes, along <206> crystallographic directions, by a pure shear mechanism along the edge of the octahedral copper-oxygen units. The line defects are partial screw dislocations, with characteristic displacement vectors of the type <(a/2), 0, (c/6)>, bounding the stacking faults. The existence of this type of defect demonstrates that there is an oxygen deficiency within the CuO_2 layers. However, unlike the open ReO_3 type–related structures, the packing density of the K_2NiF_4 structure necessarily requires that anion defects be accompanied by the loss of cations of the A type (lanthanum, strontium). Under identical synthesis conditions, no defects are observed in the parent compound La_2CuO_4.

ALL OF THE HIGH-TEMPERATURE, copper oxide–based superconductors discovered so far have CuO_2 sheets as a common structural feature, and these are believed to play a key role in the high-temperature superconductivity. There have been numerous reports of the structural, physical, and electronic properties in the La-Cu-O system partially substituted by Ba and Sr (*1–5*). The parent La_2CuO_4 has a distorted K_2NiF_4 structure with an orthorhombic cell (a = 5.36 Å, b = 5.41 Å, and c = 13.17 Å). It consists of corner-shared CuO_6 octahedra intersected by La–O layers (*2*), forming intergrowths of single $(CuO_2)^{2-}$ sheets alternating with $(La_2O_2)^{2+}$ (001) double layers with the rock salt structure. The structure has two long Cu–O distances (~2.4 Å) along the c axis and four short Cu–O distances (~1.9 Å) along the a and b axes; the average Cu–O distance may be regarded as ~2 Å (*2*). The Cu–O sheets are buckled and the octahedra are alternately rotated, causing distortions (*2*). Figure 1A shows the structural projection, ignoring the distortions, tilted along the [110] direction from [010]. Partial substitution of Sr for La in the structure oxidizes the CuO_2 sheets and raises the average formal oxidation state of Cu. A tetragonal, O-deficient K_2NiF_4 structure (*2*) is obtained for $x > 0.05$ (Fig. 1B, which is modeled on Fig. 1A). Superconductivity is realized at Sr concentrations of $0.05 < x < 0.25$ (*3*).

The transition temperature (T_c) of $La_{2-x}Sr_xCuO_4$ varies with Sr content, approaching a maximum value of ~37 K at x = 0.15 and falling off sharply on either side of this value of x (Fig. 2) (*3, 6*). The rise in T_c toward x = 0.15 is attributed to an increase in the formal oxidation state of Cu (hole content) (*3*). The effect of possible O defects on superconducting properties for x = 0.15 has also been described; these results are based on differential thermal analysis measurements (*7*). The evolution of the microstructural changes and the associated microchemistry, as a function of Sr content, could also play an important role. However, such studies on defect structures in noncubic materials and, in particular, in tetragonal systems are very limited.

Samples of $La_{2-x}Sr_xCuO_4$ with x = 0.05, 0.075, 0.11, 0.15, and 0.225 were prepared by standard solid-state techniques with stoichiometric quantities of La_2O_3, CuO, and SrO_2 (*6*). Well-ground mixtures of the binary oxides were fired at 1100°C in an O_2 atmosphere for 12 hours and then furnace-cooled to room temperature. The samples were reground and refired under the same conditions to ensure complete reaction. Powder x-ray diffraction data were collected for each sample, and by this criteria all of them appeared to be single phase. Refined tetragonal unit cell parameters (with space group *I4/mmm*) are listed in Table 1. The transition temperatures (Fig. 2) were obtained for the Sr-doped samples with a superconducting quantum interference device (SQUID) (*6*).

Five samples were studied in detail by transmission electron microscopy (TEM): the parent La_2CuO_4 and $La_{2-x}Sr_xCuO_4$ with nominal compositions of x = 0.05, 0.075, 0.15, and 0.225. In each case, the crystallites were ultrasonically dispersed in chloroform and suspended on C-filmed Al grids. To avoid introducing or modifying defects, we prepared the samples without any mechanical treatment such as grinding. The use of a Philips 300-kV TEM, fitted with a low-light-level television camera, made it possible to examine the resulting

Table 1. Refined tetragonal unit cell parameters (a and c) of $La_{2-x}Sr_xCuO_4$ as a function of x. The values in parentheses are the estimated standard deviations in the refinement of the powder x-ray spectra. Three samples of each composition were studied.

x	a (Å)	c (Å)	Volume (Å^3)
0.075	3.7829(8)	13.188(3)	188.73
0.150	3.7717(8)	13.226(3)	188.15
0.225	3.7649(7)	13.240(3)	187.67

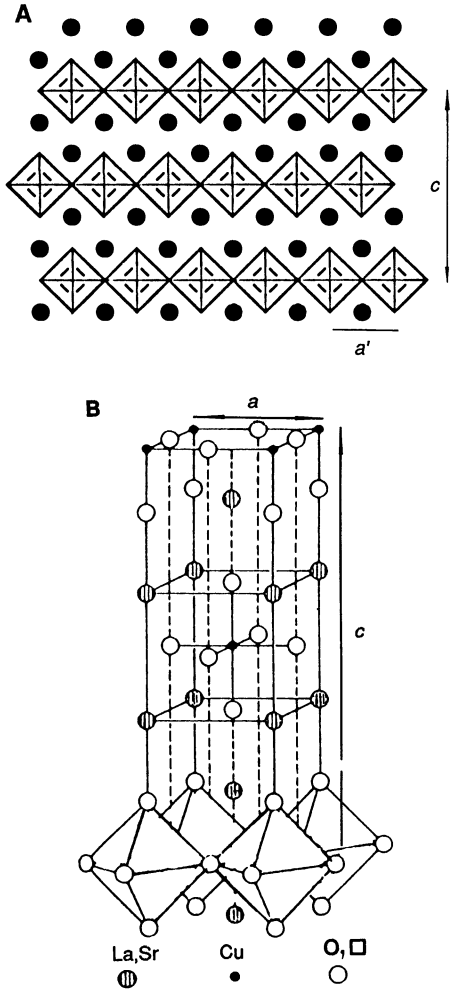

Fig. 1. Idealized structures of (**A**) La_2CuO_4 tilted along the [110] projection; (**B**) O-deficient, tetragonal K_2NiF_4 structure of $La_{2-x}Sr_xCuO_4$ ($x > 0.05$) in the [010] projection with the c axis vertical; (B) is related to (A): $a' = a_{ortho}/\sqrt{2}$. The lattice parameters are given in Table 1.

Central Research and Development Department, E. I. DuPont de Nemours Inc., Experimental Station, Wilmington DE 19880.

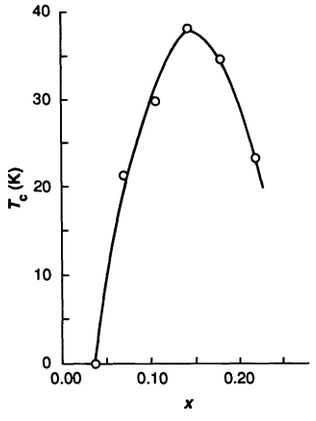

Fig. 2. Plot of T_c versus x for $La_{2-x}Sr_xCuO_4$.

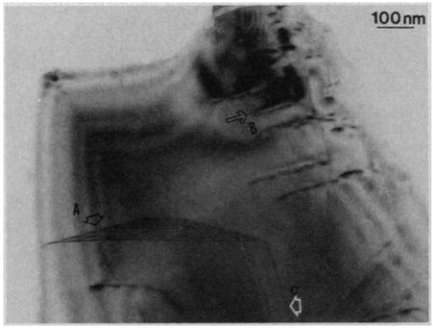

Fig. 3. Shorter defects and stacking fault contrast (at A, extending to the surface), in the $x = 0.05$ sample. Another stacking fault (at C), which is normal to it, lies in the crystal. The characteristic black-white contrast of the defects (arrowed at B) indicates that the defects are close to the surface of the crystal. (Diffraction contrast, bright field; **g** = 013 reflection.)

thicker crystals. Low electron beam currents were used to minimize any damage, and the samples were found to be quite stable under the beam. Samples of the simple La_2CuO_4 compound, prepared by identical procedures, did not exhibit any defect structures similar to those found reproducibly in the Sr-doped materials. The defect density also increased with Sr content up to $x = 0.15$. We concluded that the defects are in the original crystals as a direct consequence of the Sr doping. They are not due to the subsequent procedures used to prepare specimens for TEM. We confirmed the chemical composition of each thin EM sample, on a microscale, by high–spatial resolution chemical microanalysis from 30 selected areas, each ~0.1 μm in extent, using energy-dispersive x-ray spectrometry (EDX).

The defects were characterized by the conventional diffraction contrast technique (*8*). In this technique, a single Bragg beam is excited and contrast is produced by the use of either the transmitted beam (bright field) or the diffracted beam (dark field). In the high-resolution EM (HREM) method of lattice imaging, two or more Bragg reflections are used. However, reliable and unambiguous interpretation of defect structures with HREM is often extremely difficult, because the images depend very sensitively on microscope parameters such as defocus, astigmatism, and aberration of lenses; extensive computer modeling is essential (*8*).

Imaging of defects to analyze their character by the use of diffraction contrast depends on being able to tilt the specimen in the TEM very accurately; accurate tilt is made possible with information derived from small-area diffraction patterns, which achieves exact diffracting conditions locally. Crystals several micrometers wide, but only a few tens of nanometers thick, were chosen for these experiments. Selected-area diffraction was used to orient the crystals with optimized small deviations from the exact Bragg angles (*9*). The Burgers displacement vector **b** of the defect characterizes the defect and provides the magnitude of the displacement associated with it; we determined **b** by tilting the crystal to a series of orientations with Bragg reflections **g** excited. There are established criteria for this procedure (*8*). It is necessary to achieve zero contrast in the image in at least one, and usually several, reflections. This zero contrast is obtained when the displacements are parallel to the reflecting plane and there is no interaction between the diffraction and displacement vectors, that is, the dot product $\mathbf{g} \cdot \mathbf{b} = 0$. The dislocation becomes invisible, with zero contrast.

There may be some residual contrast if the elasticity is not completely isotropic, or if, as in this case, **b** of the dislocation is not quite normal to the low-index **g** used to establish the definitive imaging conditions. Nevertheless, a knowledge of the possible crystallography of the defects can be used to set up a series of images to obtain a unique solution for **b** for each segment of the defect. One can determine the character of the defect, for example, whether it is an edge or a screw dislocation, by relating the diffraction analysis of **b**, in reciprocal space, with the orientation of the line, or plane, of the defect in real space. In the TEM there is an accurately calibrated rotation of the diffraction pattern, with respect to the image. In general, the conditions for imaging the partial dislocations bounding each edge of a stacking fault are different from those needed to image the stacking fault contrast itself.

The La_2CuO_4 sample was found to consist of well-ordered single crystals without any discernible pattern of extended defects. Microanalysis confirmed the cation stoichiometry. In addition, samples with $x = 0.05$, 0.075, and 0.15 exhibited two sets of extended defects almost normal to each other. The defects were found to be a general phenomenon in the samples. The dark line images of the defects were similar in these samples: but the density of these defects was much greater in the sample with $x = 0.15$, which has a high Sr content. In the samples with Sr < 0.075, the defects were found to

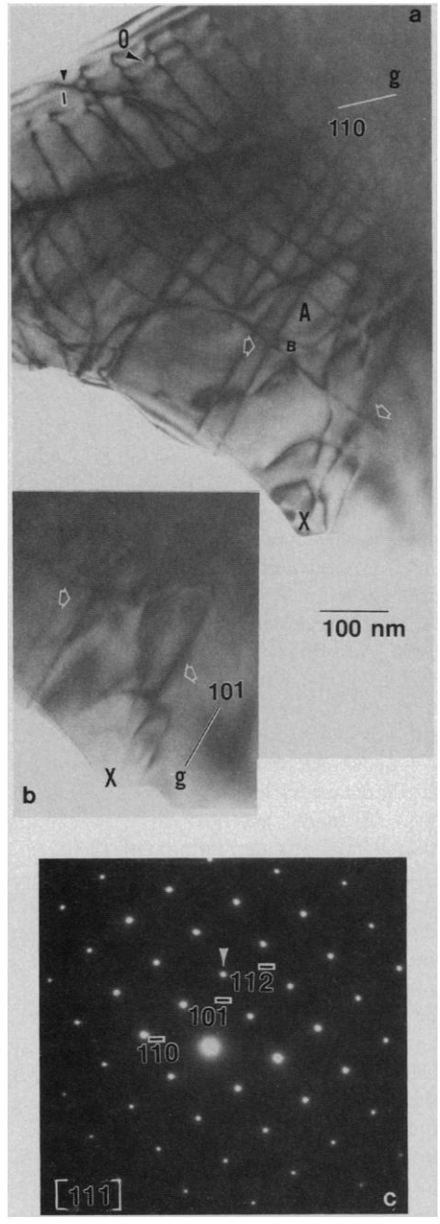

Fig. 4. (**a**) Two sets of extended dislocations in $La_{2-x}Sr_xCuO_4$ ($x = 0.15$) (dark lines) are along <101> directions (for example, at A and B, which are nearly normal to one another): operating reflection is **g** = (110) systematic. (**b**) One set of dislocations lies parallel to <101>, **g** = (101), and the other set [at B in (a)] is invisible. Their lengths vary between 0.5 and 0.75 μm. Oscillatory effects (at O) at the images were also observed. Crystal thickness, ~100 nm. (**c**) Electron diffraction pattern in the [111] projection with some of the reflections indexed.

be shorter and less numerous. The characteristic black-white contrast (indicated by the arrow at B in Fig. 3), is typical of that from a dislocation close to the surface of the crystal (*8*). Stacking fault contrast can be seen at A.

Figure 4a shows the two sets of defects in the $x = 0.15$ material, imaged in the two-beam case, in the [111] crystal projection with the $\mathbf{g} = (110)$ systematic reflection. Under these conditions the contrast from both sets of defects was similar. The (101) reflections are parallel to the line traces of the dislocations (Fig. 4b). The symmetry-related, near-orthogonal set of defects (for instance, at B in Fig. 4a) is invisible in the (101) reflection in Fig. 4b. When dislocations normal to each other intersect, their strain fields interact and produce buckling in the image (for example, at A in Fig. 4a). Diffraction patterns recorded from this area show two sets of faint diffuse streaks in directions normal to the defects and originating from the defect strain fields. The streaks suggest that the extended defects are not ordered and the necessary transport properties are not sufficiently facile to impose ordering. If they were ordered, a crystallographically defined compound with a definite composition might be obtained. An indexed [111] diffraction pattern is shown in Fig. 4c. Detailed contrast experiments, carried out in the EM, established that the dislocations were on {010} (or {100} type) planes. For these dislocations the vanishing criterion was satisfied in $\mathbf{g} = (011)$ [which is nearly normal (~86°) to (101)], and the dislocation line was parallel to $\mathbf{g} = (101)$. For those dislocations associated with the symmetry-related orthogonal defects on (011), $\mathbf{g} \cdot \mathbf{b} \sim 0$ contrast was achieved with $\mathbf{g} = (101)$, as shown in Fig. 4b. The dislocations in $\mathbf{g} = (010)$ or (100) were invisible. The EDX results showed an Sr deficiency of up to 10% in the sample. An La deficiency was also observed, but the concentration could not be deduced to the same accuracy. In addition, EDX showed a few grains of the unreacted component oxides in the sample.

The analysis of the contrast data gave a pure shear displacement with dislocations of almost pure screw character, that is, with the direction of the dislocation line close to that of the displacement vector. The (101) defect images had narrow single peaks in data obtained with $\mathbf{g} = (110)$, (220), and (100). From the contrast experiments the Burgers vectors for the dislocations associated with each set of defects were determined to be of the type $\mathbf{b} = \langle(a/2), 0, (c/6)\rangle$ and $\langle 0, (b/2), (c/6)\rangle$ in the real structure. In the tetragonal unit cell with lattice parameters $a = b << c$, these two values of $\mathbf{b}$ are crystallographically equivalent. The indices of $\mathbf{b}$ are in direct proportion to the extended c/a ratio for this crystal structure [$c/a = 3.5$]. Defects along the two equivalent directions meet at an acute angle of ~86°.

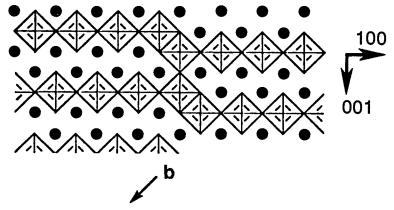

Fig. 5. A possible model for the shear defect and the stacking fault, in $La_{2-x}Sr_xCuO_4$, by shear along a CuO_6 octahedron edge [with a displacement $(1/2)a + (1/6)c$] eliminating point defect vacancies, $(0.05 \leq x \leq 0.15)$. The (La, Sr) atoms behind and above the sheared octahedra are not shown. The two sheets of octahedra in the alternate layers shown are at different levels in the structure. The direction of the shear and the magnitude were obtained from electron microscopy.

The defects with $\mathbf{b} = \langle(a/2), 0, (c/6)\rangle$ are partial screw dislocations in the perfect structure separating a stacking fault. By definition, a partial (that is, not complete) dislocation has a stacking fault on one side of it and the stacking fault is terminated by the dislocation. If we ignore the distortion of the octahedra in the bulk structure, the nature of the planar stacking fault can be modeled by a shear (which converts corner-shared to edge-shared CuO_6 octahedra), along the edge of a CuO_6 octahedron, as indicated for alternate layers, by the arrow in Fig. 5. The shear mechanism forming the dislocations implies vacancies: O point defects and cation deficiency associated with the loss of (La, Sr). The octahedra across the fault share edges instead of just corners, as in the perfect structure. Thus, along the defects there are local changes in the coordination of O to metal atoms, resulting in deviations from the ideal stoichiometry. The defects modify the Cu^{111} content and can have a direct influence on the superconducting properties. A schematic representation of the stacking fault bounded by partial dislocations in the tetragonal system is shown in Fig. 6 (top). The model used to interpret characteristic black-white contrast effects (in Fig. 3) is shown in Fig. 6 (bottom): a partial screw dislocation bounds a stacking fault extending to the surface. It is probable that the defects are introduced to accommodate lattice strains resulting from the structural changes and the point defects associated with the substitution of the larger Sr^{2+} for La^{3+}. It remains to be seen whether the coherent intergrowths consisting of slabs of corner-sharing perovskite blocks separated by units of the NaCl structure type, reported in the La-Cu-O series (*10*), are evolved by such a polyhedral shear process.

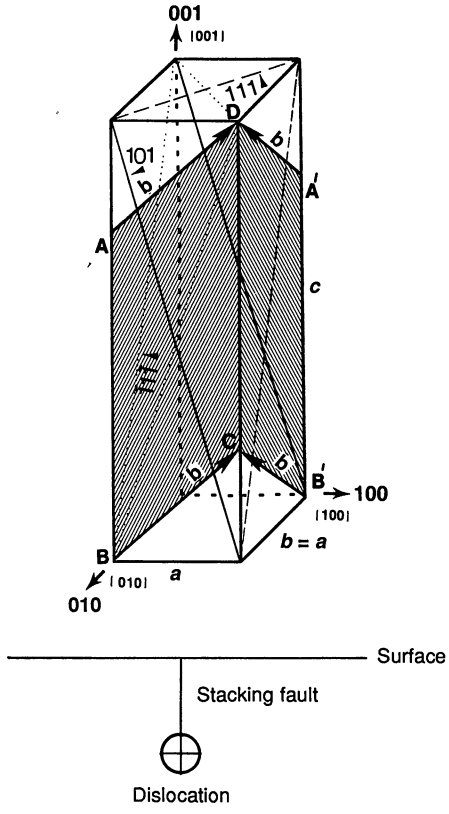

Fig. 6. (**Top**) Schematic representation of the shear defect and the stacking fault geometry in the tetragonal La-Sr-Cu-O system ($c/a = 3.5$). The stacking faults are shaded regions ABCD and A'B'CD, and lie in (010) and (100) planes. The faults ABCD and A'B'CD are bounded by two sets of partial dislocations, with characteristic displacement vectors $\mathbf{b} = \langle(a/2), 0, (c/6)\rangle$ and $\langle 0, (b/2), c/6)\rangle$, respectively, as shown. The dislocations are along <206> (or <103>) and <026> (or <013>) directions, respectively. Some of the (101) and (111) planes are indicated. (**Bottom**) Model used to interpret the characteristic black-white contrast effects, and the stacking fault, A in Fig. 3. A partial screw dislocation bounds a stacking fault that extends to the surface.

The dislocations reported here have almost pure screw character, and this type of dislocation can be nucleated directly by the formation of a small shear loop in the presence of shear strains arising from the structural modifications due to substitution. Alternatively, the dislocations might be nucleated as small collapsed disks due to shear (*9, 11*), part of the loop then expanding by a lattice strain–driven glide mechanism on the (010) planes containing the dislocations. On average, one line defect per 40 unit cells was observed in the $x = 0.15$ sample. This would indicate the anion deficiency associated with the extended defects in the sample to be ~0.025, and in the sample with $x = 0.05$ to be ~0.01, with similar estimates for cation defects (on the assumption of the loss of an anion and an A cation per unit cell in the proposed model). These

estimates may relate only to the supersaturation, and there will also be an equilibrium background concentration of point defects in the material.

The proposed model for shear indicates that the stacking faults lie in the (010) [or the symmetry-related (100)] planes, bounded by partial screw dislocations with $\mathbf{b} = <(a/2), 0, (c/6)>$ or $<0, (b/2), (c/6)>$. Accurate analysis of the habit plane of the stacking faults was not possible because of limited tilt (±10°) in the TEM. The fault displacement vector **R** (by which the crystal above and below the fault is displaced) is of the type 1/2 [010]. Stacking fault contrast can be revealed with the use of appropriate reflections so that $\mathbf{g} \cdot \mathbf{R}$ is not an integer (*8*), as shown in Fig. 3. The samples with $x = 0.225$ showed chemical inhomogeneity and no evidence for the line defects. The type of shear reported here could also be present in other Cu–O sheet, high-temperature superconductors, including those with the square pyramidal units.

REFERENCES AND NOTES

1. J. G. Bednorz and K. A. Muller, *Z. Phys. B* **64**, 189 (1986).
2. J. M. Longo and P. M. Raccah, *J. Solid State Chem.* **6**, 526 (1973); V. B. Grande *et al.*, *Anorg. Allgemeine Chem.* **428**, 120 (1977); C. Michel and B. Raveau, *Rev. Chim. Mineral.* **21**, 407 (1984).
3. J. B. Torrance *et al.*, *Phys. Rev. Lett.* **61**, 1127 (1988).
4. P. Day *et al.*, *J. Phys. C* **20**, L429 (1987).
5. J. B. Goodenough and A. Manthiram, *Physica C* **157**, 439 (1989).
6. M. K. Crawford, W. E. Farneth, E. M. McCarron III, *Phys. Rev. B*, in press.
7. J. M. Tarascon, L. H. Greene, W. R. McKinnon, G. W. Hull, T. H. Geballe, *Science* **235**, 1373 (1987).
8. P. B. Hirsch *et al.*, *Electron Microscopy of Thin Crystals* (Krieger, Melbourne, FL, 1977).
9. P. L. Gai, W. Thoeni, P. B. Hirsch, *J. Less Common. Met.* **56**, 263 (1979).
10. A. H. Davies and R. J. Tilley, *Nature* **326**, 859 (1987).
11. L. Kihlborg, *Ark. Kemi* **21**, 443 (1963).

12. We are indebted to A. W. Sleight, C. C. Torardi, and E. D. Boyes for helpful discussions and for a critical reading of the manuscript. The assistance of L. G. Hanna, D. L. Smith, and I. R. Hartmann with the EM is gratefully acknowledged.

7 August 1989; accepted 16 November 1989

An Empirical Model of Total Solar Irradiance Variation Between 1874 and 1988

P. FOUKAL AND J. LEAN

An empirical model of variations in the total solar irradiance caused by observed changes in photospheric magnetic activity between 1874 and 1988 is presented. The model provides a remarkably good representation of the irradiance variations observed by satellite-borne radiometers between 1980 and 1988. It suggests that the mean total irradiance has been rising steadily since about 1945, with the largest peak so far at about 1980 and another large peak expected during the current solar cycle 22. But it is doubtful whether even this rise can contribute significantly to global warming, unless the temperature increase of about 0.02°C that it produces in current energy balance models seriously underestimates the sensitivity of climate to solar irradiance changes.

RADIOMETRIC DATA FROM THE Solar Maximum Mission (SMM) and Nimbus-7 satellites have shown that the total solar irradiance declined by about 0.1% between solar activity maximum in about 1981 and minimum activity in 1986 and has since risen with increasing activity in the new sunspot cycle 22 (*1*). Most of this brightening of the active sun can be attributed to the irradiance effect of photospheric magnetic structures called faculae, whose areas increase at times of high sunspot number (*2*). Contributions from changes in the total irradiance not directly associated with photospheric magnetic activity have also been suggested (*3*).

The mechanism responsible for the total irradiance variation is of interest in examining possible influences of solar radiative output on climate. Climate models indicate that an irradiance variation of the magnitude observed over the last 11 years is too small to have significant impact on global temperature (*4*). However, a variation of this size occurring over many decades might contribute at an appreciable level to trends that may have occurred over the past century. We describe here an empirical model of total solar irradiance variation over the period from 1874 to 1988, developed from our understanding of the irradiance variation that has been directly observed since 1978.

In previous work (*2*), we have shown that after correction for the dimming caused by dark sunspots the total solar irradiance variations observed between 1981 and 1984 by the Active Cavity Irradiance Monitor (ACRIM) on SMM and the Earth Radiation Budget (ERB) radiometer on Nimbus 7 can be reconstructed from observed variations in facular area. The correction for sunspot dimming was computed from daily positions and areas of spots and from their photometric contrast. We used daily values of the He I index, a measure of the area of faculae on the entire disk including both magnetically active and quiet regions, as the basis for our reconstruction of the facular irradiance effect.

P. Foukal, Cambridge Research and Instrumentation, Inc., Cambridge, MA 02139.
J. Lean, E. O. Hulburt Center for Space Research, Naval Research Laboratory, Washington, DC 20375.

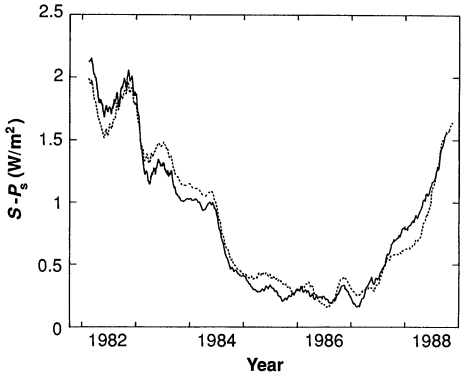

Fig. 1. A comparison of the ACRIM irradiance residuals (solid line) for 1982 to 1988 with a reconstruction of the irradiance residuals (dotted curve) based on the use of the linear regression given in the text. An 81-day smoothing has been applied to the data.

We show here that our irradiance variation model successfully represents the radiometry over the interval from 1980 to 1988 covered by the available ACRIM data. In the present study we use the solar Lyman alpha (Lyα) flux (*5*) as an index of facular area instead of the He I index. The Lyα radiation of faculae arises from layers of the solar atmosphere relatively close to the photospheric layers that emit most of the sun's radiative output. The Lyα flux is less influenced than the He I emission by radiations from the very hot overlying coronal layers that contribute negligibly to the total solar irradiance. Also, we use the ACRIM radiometry alone in this paper to simplify the presentation, although the conclusions we reach are equally valid for a parallel analysis that we have carried out on the ERB data.

The irradiance residuals, $S - P_s$ (where S is the total irradiance measured by the ACRIM radiometer and P_s is the correction for sunspot dimming), are found to increase